Kinematic and Static Analyses of a 3-DOF Spatial Tensegrity Mechanism

Karol Muñoz, Mathieu Porez, Philippe Wenger

Kinematic and Static Analyses of a 3-DOF Spatial Tensegrity Mechanism

Karol Muñoz, Mathieu Porez and Philippe Wenger

Nantes Université, École Centrale Nantes, Institut Mines Télécom Atlantique, CNRS, LS2N, UMR 6004, F-44000 Nantes, France
{karol.munoz-salas@ls2n.fr,mathieu.porez@imt-atlantique.fr,philippe.wenger@ls2n.fr}

Abstract. This paper proposes a new light-weight spatial tensegrity joint mechanism to be used in serial manipulators. The mechanism uses a simple architecture of bars, cables, platforms and spherical joints, making it lightweight and suitable for integration into a stack of robot designs. We start with a 3-degree-of-freedom (DOF) mechanism actuated by 3 cables and we add an additionnal passive cable taught at a suitable tension to ensure stability and to limit the number of DOF to 2.

Keywords: Cobots, tensegrity, spatial mechanism, kinematic analysis, static analysis, stability

1 Introduction

Robotics, especially collaborative industrial robots (cobots), has emerged as a key driver in this new industrial era [1]. However, the versatility of these cobots comes with inherent risks. Substantial differences in mass and rigidity mean that a collision between a cobot and a human could have fatal consequences [2]. To ensure operator safety and optimize the benefit-risk ratio of utilizing robotics in industry, innovative adaptive kinematics for robots must be proposed. These kinematics should strike a balance between being sufficiently rigid for precise operation in a confined workspace and flexible enough to move safely within the area occupied by an operator [3]. In addressing this challenge, our focus is on tensegrity mechanisms. Tensegrity structures emerged as a design trend in the 1960s [4–6], and over time their application has spread to various fields [7]. Robotics is one such area where numerous studies have been conducted, as highlighted by Liu et al. in their research [8]. Other examples of robotic applications using tensegrity include deployable robots [9], mobile robots [10], and manipulator robots [11, 12]. Tensegrity systems offer tunable geometric configuration, rigidity, and stability by adjusting cable tension through co-actuation. This potential makes tensegrity promising for designing robots with both precision rigidity and flexible collaboration with human operators. Burkhardt [13] introduced the T-prism, a basic 3-D tensegrity structure. This research explores its construction using dowels, fishing lines and cylindrical coordinates. The optimisation problem minimises the length of the side tendons while satisfying radius, strut length and symmetry constraints. Arsenault and Gosselin [14] proposed a 3-DOF positional tensegrity mechanism with a modular design, reduced inertia, and a large

workspace. It is treated as an assembly of independent elements based on Snelson's X-shaped tensegrity system [6]. The limits of the actuator workspace reveal limitations for mechanisms with three or more modules. Marshall [15] introduced a parallel platform device based on tensegrity principles. It replaces elements with variable length legs and combinations of springs and connectors. The analysis confirms the configurability of the upper platform by externally applied wrench coordinates. Furet [16] and Fasquelle [17] use antiparallelogram tensegrity joints to model a bird neck. Mirats and Camps [18] proposed a tensegrity-based robot with a 3-bar symmetric prismatic configuration. Despite being underactuated, controlled motion is achieved within its workspace. The study anticipates future work on control laws and hyper-actuated structures. Kim [19] proposed a compact 2-DOF cable-driven wrist joint. John [20] noticed that this wrist joint has theoretical mobility of 0 and that the practical mobility is only provided by link deformations and clearances. He then proposed a new variant to overcome this issue. Their work presents a new variant of the quaternion joint and contributes to the advancement of tensegrity-based robotic manipulators in bio-inspired robotics.

Based on this research, the left side of Fig. 1 illustrates our proposed spatial mechanism, meanwhile, the right side of the same figure shows a robotic manipulator formed by stacking the proposed mechanism. This article will focus on the study of the proposed spatial mechanism, with future efforts aimed at exploring the implications of stacking this mechanism to form a robotic manipulator.

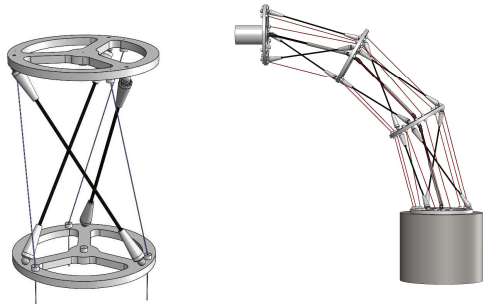

Fig. 1: CAD modelling of the spatial mechanism and robot design using a stacked configuration.

The proposed mechanism design (see Fig. 1 left) introduces a simple and lightweight configuration. This stands in contrast, for example, to Marshall's study, which involves the use of linear actuators and motors in the same mechanism, potentially increasing its weight [15]. Instead, our design consists solely of bars, cables, and spherical joints. However, it is essential to ensure that the forces within the bars are in compression and the cable forces are in tension to maintain tensegrity conditions. Together, these features make it an interesting proposal with the potential to optimize the human-machine workspace.

2 Geometry of the mechanism

Fig. 2 illustrates the parameterization of the 3-DOF spatial manipulator. The mechanism consists of a fixed lower platform, a mobile upper platform, three bars, and three cables. While the manipulator initially offers 6-DOF, the presence of the three bars imposes three constraint forces, resulting in a 3-DOF spatial manipulator.

The fixed platform features vertices $A_1, B_1, A_2, B_2, A_3, B_3$, while the mobile upper platform features vertices $A_4, B_5, A_5, B_6, A_6, B_4$. The equidistant centres for the platforms are denoted o_0 and o_3 respectively. The points A_i are placed at a uniform distance b from each other, forming an angle ψ between A_i and B_i in the lower platform and $-\psi$ for the upper platform. The platforms are interconnected by three equal-length bars, designated as L, which link A_1 to A_6, A_3 to A_5, and A_2 to A_4. Additionally, the mechanism comprises three cables of lengths l_1, l_2, and l_3, connecting B_1 to B_4, B_2 to B_5, and B_3 to B_6, respectively. Three reference frames are defined: $\mathcal{F}_g = (o_g, \mathbf{s_g}, \mathbf{n_g}, \mathbf{a_g})$, $\mathcal{F}_0 = (o_0, \mathbf{s_0}, \mathbf{n_0}, \mathbf{a_0})$, and $\mathcal{F}_3 = (o_3, \mathbf{s_3}, \mathbf{n_3}, \mathbf{a_3})$, as visualised in Fig. 2. Here $\mathcal{F}_g$ represents the general reference frame, $\mathcal{F}_0$ is fixed to the lower platform and $\mathcal{F}_3$ is on the upper platform. Since the proposed mechanism is designed to be used as a joint in a series arrangement of such mechanisms (see Fig. 1, right), two angular parameters α and β (see Fig. 2, bottom right) are used to define its orientation in space.

We use tilt and torsion angles [21] to parametrize the orientation of the moving platform w.r.t. its base. As shown in Fig. 2, the rotation matrix ${}^0R_3$ between $\mathcal{F}_0$ and $\mathcal{F}_3$, which defines the 3-D orientation for the mobile platform at o_3 in Cartesian space, is given by:

$$ {}^0R_3 = \mathrm{rot}(a_0, \phi)\mathrm{rot}(n_1, \theta)\mathrm{rot}(s_2, \sigma - \phi), \tag{1} $$

where these three unit rotations around a_0, n_1 and s_2 define the tilt for the first two and the torsion for the last one.

Table 1 presents the parameters and their respective values that are asigned to the mechanism as shown in Fig. 2 and utilized throughout the process.

Table 1: Parameters, symbols and values for the proposed mechanism.

Parameter	Symbol	Value
Distance between points A_i	b	15 cm
Angle between A_i and B_i	ψ	15° ($\pi/12$ rad)
Length of the bars	L	30 cm
Diameter of the bars	D_b	0.5 cm
Mass of the mobile platform	m	50 g

3 Kinematic analysis of the mechanism

We formulate the inverse kinematic model, which is obtained in two steps. The first one, called trilateration, involves computing the coordinates of the top platform $(X, Y, Z)^T$ in

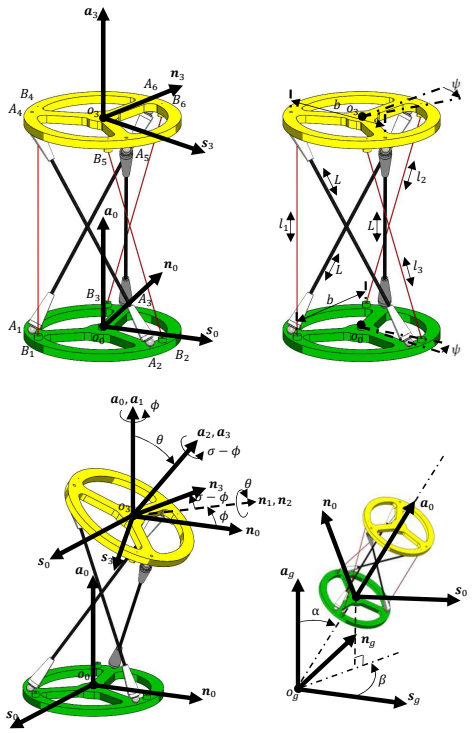

Fig. 2: Parameters of the mechanism.

the frame $\mathcal{F}*_3 = (o_o, \mathcal{B}_3)$, where $\mathcal{B}_3$ is the vector base $(\mathbf{s_3}, \mathbf{n_3}, \mathbf{a_3})$ (Fig. 2). The second step is to determine the cable lengths l_i based on the spatial angles (ϕ, θ, σ). To derive the position of the upper platform as a function of spatial angles, we consider the three geometric constraints imposed by the legs on the upper platform, namely $L^2 = ||A_1A_6||^2$, $L^2 = ||A_2A_4||^2$ and $L^2 = ||A_3A_5||^2$. In terms of $(X, Y, Z)^T$, these constraints can be expressed as:

$$\begin{pmatrix} 1 & 1 & 1 \\ 1 & 1 & 1 \\ 1 & 1 & 1 \end{pmatrix} \begin{pmatrix} X^2 \\ Y^2 \\ Z^2 \end{pmatrix} - 2 \begin{pmatrix} x_{\mathcal{S}_1} & y_{\mathcal{S}_1} & z_{\mathcal{S}_1} \\ x_{\mathcal{S}_2} & y_{\mathcal{S}_2} & z_{\mathcal{S}_2} \\ x_{\mathcal{S}_3} & y_{\mathcal{S}_3} & z_{\mathcal{S}_3} \end{pmatrix} \begin{pmatrix} X \\ Y \\ Z \end{pmatrix} + \begin{pmatrix} x_{\mathcal{S}_1}^2 + y_{\mathcal{S}_1}^2 + z_{\mathcal{S}_1}^2 - L^2 \\ x_{\mathcal{S}_2}^2 + y_{\mathcal{S}_2}^2 + z_{\mathcal{S}_2}^2 - L^2 \\ x_{\mathcal{S}_3}^2 + y_{\mathcal{S}_3}^2 + z_{\mathcal{S}_3}^2 - L^2 \end{pmatrix} = 0, \tag{2}$$

where $o_{s1} = (x_{\mathcal{S}_1}, y_{\mathcal{S}_1}, z_{\mathcal{S}_1})^T$, $o_{s2} = (x_{\mathcal{S}_2}, y_{\mathcal{S}_2}, z_{\mathcal{S}_2})^T$ and $o_{s3} = (x_{\mathcal{S}_3}, y_{\mathcal{S}_3}, z_{\mathcal{S}_3})^T$ are the coordinates of the centres of the three spheres denoted $\mathcal{S}_1$, $\mathcal{S}_2$ and $\mathcal{S}_3$, each with a radius of L, intersecting at o_3. To solve (2), we use the trilateration method like the work of Stock [22]. Considering the three circles coming from the intersection of the spheres and the plane containing the upper platform, from (2), the equation of the circle C_i coming from $\mathcal{S}_i$ is the following:

$$\rho_i^2 = (X - x_{\mathcal{S}_i})^2 + (Y - y_{\mathcal{S}_i})^2, \tag{3}$$

where $\rho_i^2 = L^2 - Z^2 + 2Zz_{0i} - z_{0i}^2$ is the radius of the circle $\mathcal{S}_i$. Subtracting the equation of C_3 from those of C_1 and C_2 gives the following linear system:

$$\begin{pmatrix} A_{11} & A_{12} \\ A_{21} & A_{22} \end{pmatrix} \begin{pmatrix} X \\ Y \end{pmatrix} = \begin{pmatrix} B_1 \\ B_2 \end{pmatrix} Z + \begin{pmatrix} C_1 \\ C_2 \end{pmatrix}, \tag{4}$$

where $A_{11} = x_{\mathcal{S}_1} - x_{\mathcal{S}_2}$, $A_{12} = y_{\mathcal{S}_1} - y_{\mathcal{S}_2}$, $A_{21} = x_{\mathcal{S}_1} - x_{\mathcal{S}_3}$, $A_{22} = y_{\mathcal{S}_1} - y_{\mathcal{S}_3}$, $B_1 = 2(z_{\mathcal{S}_2} - z_{\mathcal{S}_1})$, $B_2 = 2(z_{\mathcal{S}_3} - z_{\mathcal{S}_1})$, $C_1 = x_{\mathcal{S}_1}^2 - x_{\mathcal{S}_2}^2 + y_{\mathcal{S}_1}^2 - y_{\mathcal{S}_2}^2 - z_{\mathcal{S}_2}^2 + z_{\mathcal{S}_1}^2$, and $C_2 = x_{\mathcal{S}_1}^2 - x_{\mathcal{S}_3}^2 + y_{\mathcal{S}_1}^2 - y_{\mathcal{S}_3}^2 - z_{\mathcal{S}_3}^2 + z_{\mathcal{S}_1}^2$. The solution of (4) is:

$$X = \alpha_X Z + \beta_X, Y = \alpha_Y Z + \beta_Y, \tag{5}$$

where $\alpha_X = (A_{22}B_1 - A_{12}B_2)/\det(A)$, $\beta_X = (A_{12}C_2 - A_{22}C_1)/\det(A)$, $\alpha_Y = (A_{11}B_2 - A_{21}B_1)/\det(A)$, and $\beta_Y = (A_{11}C_2 - A_{21}C_1)/\det(A)$. Replacing, in the equation of C_3, X and Y by the solution pair (5), we obtain a second order equation in Z, i.e.:

$$\begin{aligned} 0 = {} & (1 + \alpha_X^2 + \alpha_Y^2)Z^2 \\ & + 2(\alpha_X(\beta_X - x_{\mathcal{S}_1}) + \alpha_y(\beta_y - y_{\mathcal{S}_1}) - z_{\mathcal{S}_1})Z \\ & + ((\beta_X - x_{\mathcal{S}_1})^2 + (\beta_Y - y_{\mathcal{S}_1})^2 + z_{\mathcal{S}_1}^2 - L^2), \end{aligned} \tag{6}$$

which gives two or zero solutions as a function of (ϕ, θ, σ) and the mechanism parameters b and L. In cases where the inverse kinematic model produces two solutions, we only retain the one that is technologically compatible or physically feasible. As for the cable length, their estimation is performed using the cable length equation $l^2 = \|B_4B_1\|^2$, $l^2 = \|B_5B_2\|^2$, and $l^2 = \|B_6B_1\|^2$, where B_i is estimated once X, Y, Z are known, and the values are taken by (ϕ, θ, σ).

With the inverse kinematic model, we can analyze limb interferences by calculating the distances between the bars and comparing them with a predefined threshold. The threshold is defined by the diameter of the bar D_b (see Table 1). These distances, expressed as functions of θ, ϕ, and σ, allow the identification of values for which the distance exceeds the diameter, indicating the absence of intersection. These values represent the angles at which the mechanism can move without encountering an intersection between the bars. Fig. 3 illustrates the set of collision-free σ and θ values for all possible values of ϕ (a) and the set of collision-free ϕ and θ values for $\sigma = \pi/6$ rad (b). The grey area represents reachable values, and the white area represents unreachable values. In Fig. 3a, when $\theta = 0$, two distinct zones can be observed for σ. Zone 1 ($\sigma \in [-\pi/3, 2\pi/3]$ rad) signifies the clockwise movement of the mechanism, ranging from the point where the bars intersect ($-\pi/3$ rad) to the point where the bars align in parallel ($2\pi/3$ rad). Conversely, zone 2 ($\sigma \in [2\pi/3, 5\pi/3]$ rad) is associated with the counterclockwise movement of the mechanism, spanning from the point where the bars are parallel ($2\pi/3$ rad) to the point where the bars intersect again ($5\pi/3$ rad). In Fig. 3b, it is evident that θ is constrained within the range $[-\pi/2, \pi/2]$ rad. Consequently, based on the review of the workspace, the identified operating limits are defined as follows: $\theta \in [-\pi/2, \pi/2]$ rad, $\phi \in [-\pi, \pi]$ rad and $\sigma \in [-\pi/3, 2\pi/3]$ rad and are used in the following sections.

(a) σ vs. θ for all ϕ values

(b) ϕ vs θ for $\sigma = \pi/6$ rad

Fig. 3: Kinematic workspace of the proposed spatial mechanism.

4 Static analysis and stability of the mechanism

Considering that the mechanism will be integrated into a robot manipulator, we are investigating the influence of rigid angular motions (α, β) on the structural integrity of the proposed mechanism, while keeping its internal DOF fixed ($\phi = \theta = 0$). This examination of the system under these specific conditions provides valuable insights into its equilibrium, the cable forces and allows a thorough assessment of its feasibility. This is particularly important when considering the role of the actuators and their force limitations. The equilibrium is analyzed using Newton-Euler equations, considering the forces in the bars ($\mathbf{F}_{b1}$, $\mathbf{F}_{b2}$, $\mathbf{F}_{b3}$) and in the cables ($\mathbf{F}_{c1}$, $\mathbf{F}_{c2}$, $\mathbf{F}_{c3}$), together with the gravitational force ($\mathbf{F}_g$). Solving all these equations will yield the expressions for the tension in the cables and bars (f_{c1}, f_{c2}, f_{c3}, f_{b1}, f_{b2} and f_{b3}) as shown in Muñoz et al. [23].

Before analysing the cable tension, let us look at the stability of the mechanism. As pointed out by Burkhardt [13], the stability of the proposed T-prism mechanism depends significantly on the lengths of the three end cables, each corresponding to one side. In this study, the determination of the minimum cable length for the spatial mechanism gains importance when the system is stationary and subjected only to torsional effects around the vertical axis, leading to the conclusion that $\sigma = \psi - \pi/6$ (see [23] for more details). Using the parameters given in Fig. 2 and Table 1, we find that $\psi = \pi/12$ rad; consequently, stability is achieved when $\sigma = -\pi/12$ rad.

Therefore, the relationship between the cable tensions f_{c1}, f_{c2}, f_{c3} and σ is analysed to validate the feasibility of control by actuators when $\sigma = -\pi/12$ rad. This analysis considers the simplest context where $\alpha = 0$ and $\beta = 0$. The results indicate that the system is not stable, as evidenced by an infinite increase in cable tension at $\sigma = -\pi/12$ rad. This observation suggests a singularity where cable lengths approach a minimum, rendering the system uncontrollable. It is also noted that the cable tension only satisfies the tensegrity condition within a torsional range $\sigma \in [-\pi/3, -\pi/12]$ rad, thus defining a new torsional limit.

We will now focus on analysing the behaviour of the system by selecting different torsion values in this new region, together with its rotation in 3-D space (α, β), in contrast to the previous analysis. The results, illustrated in Fig. 4, indicate that as the torsion

value σ decreases, the orientation range (α, β) also decreases proportionally (grey zone), making it impossible to achieve complete rotations in 3-D space. As mentioned earlier, this problem has not been addressed in previous research studies.

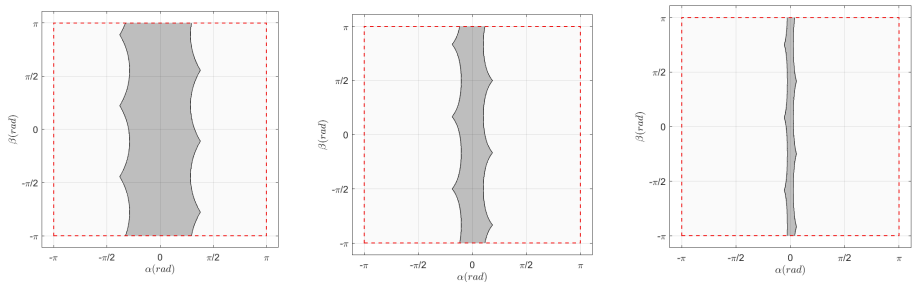

(a) $\sigma = -\pi/9$ rad (b) $\sigma = -\pi/6$ rad (c) $\sigma = -\pi/4$ rad

Fig. 4: Feasible orientation range (grey zone) for α and β with the system keeping its internal DOF fixed ($\phi = 0$ and $\theta = 0$) with different values of torsion.

To mitigate this problem and prevent cable slack, we propose to include a new central cable of length l_4, connected to o_0 and o_3, which maintains the torsional angle of the mobile platform by applying a tension to it. By including the new force $\mathbf{F}_{c4}$ in the Newton-Euler equations, a solvable linear system of equations is obtained. This leads to updated expressions for f_{c1}, f_{c2} and f_{c3} and f_{c4} is defined as the tuning parameter for the tension of the fourth cable of the mechanism. Fig. 5 illustrates the behaviour of the β vs. α region when the fourth cable is present and for different tension values for the system keeping its internal DOF fixed and $\sigma = -\pi/6$ rad. It can be seen that as the tension f_{c4} increases, the area of the β vs. α region also increases (grey zone), ensuring that f_{c1}, f_{c2} and f_{c3} are positive. Therefore, with the appropriate tension f_{c4}, the tensegrity property can be satisfied for all cable forces.

As observed in Figs. 4 and 5, the range of α and β varies as we change σ and f_{c4} respectively. It is therefore important to examine the relationship between α and β and the tension of the fourth cable (f_{c4}) and the torsion (σ). In order to identify the values of f_{c4} and σ that allow a full rotation in space while satisfying the tensegrity conditions ($\{f_{c1}, f_{c2}, f_{c3}\} > 0$) and, as a consequence, allow the use of the proposed mechanism as a stack of units for a new generation of manipulator robots.

Fig. 6 shows the result of this analysis and illustrates the limiting relationship between the tension f_{c4} and σ, ensuring a full rotation without compromising the tensegrity condition (grey area). As can be seen, an increase in the tension allows a greater range of torsional rotation where the tensegrity condition is satisfied. The figure also shows points D, E, G, which represent the values when the tension f_{c4} is equal to 1, 2 or 4 times mg respectively, in the case where the torsion considers a value of $\sigma = -\pi/6$ rad. It can be seen that points D and E are clearly outside the grey zone (area where the motion is ensured without compromising tensegrity). In the case of point F falls within the grey zone. This observation is consistent with the results shown in Fig. 5.

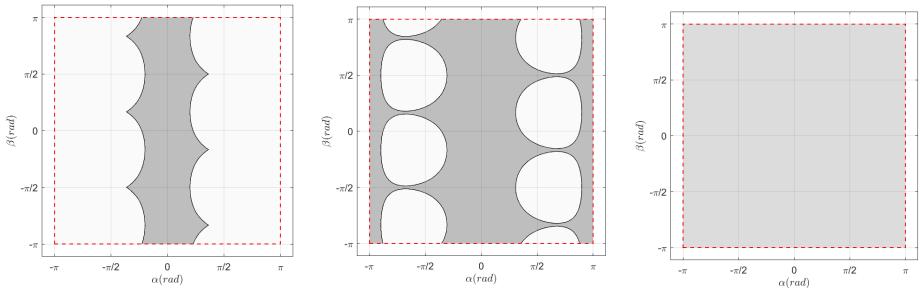

(a) $f_{c4}/mg = 1$ (b) $f_{c4}/mg = 2$ (c) $f_{c4}/mg = 4$

Fig. 5: Feasible orientation range (grey zone) for α and β with the system keeping its internal DOF fixed ($\phi = 0$ and $\theta = 0$) and torsion $\sigma = -\pi/6$ rad with different values of f_{c4}.

Also, by studying the sum of tensions ($f_{c1} + f_{c2} + f_{c3} + f_{c4}$), which is proportional to the energy consumed by the actuators to maintain the internal DOF fixed according to $f_{c4}/(mg)$ vs. σ, we aim to find the optimal value of σ where the nominal sum of tensions is minimised, as shown in Fig. 6. The optimal value of σ is $-18.1°$, corresponding to the minimum of the nominal sum of tensions ($f_{c1} + f_{c2} + f_{c3} + f_{c4}$) $= 2.20$ times mg and minimum of the nominal tension $f_{c4} = 1.16$ times mg, while satisfying the tensegrity conditions for any orientation α and β.

In conclusion, the tensegrity condition can be satisfied by adding a fourth cable between o_0 and o_3. Once this fourth cable has been added, it is essential to adjust its tension to ensure a certain torsion value (σ) and to make all the tensions f_{c1}, f_{c2} and f_{c3} of the cable forces positive.

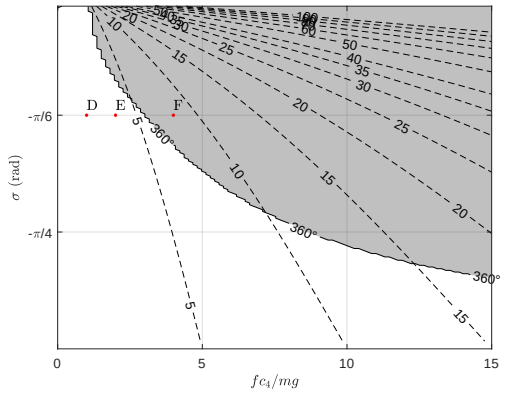

Fig. 6: Relationship between f_{c4} and σ ensuring the tensegrity condition (grey zone) for the system keeping its internal DOF fixed ($\phi = 0$ and $\theta = 0$) with angular orientations around α and β considering $(f_{c1} + f_{c2} + f_{c3} + f_{c4})/(mg)$.

5 Conclusions and future work

In this paper we propose a new design perspective based on Burkhardt's T-prism [13] and it consists of two platforms, one fixed and one mobile, connected by cables and bars. Its main advantages lie in its simplicity and lightness, which distinguishes it from previous research. These characteristics makes the mechanism suitable for the construction of collaborative robots (cobots). The mechanical integration constraint imposes a non-coincident arrangement of the cable and bar endpoints, introducing an angle between them. This feature adds an interesting aspect to the stability analysis. The analysis shows that the system encounters a singularity at a torsion value intended to achieve stability. To overcome this, the introduction of a fourth cable is proposed. Precise tuning of the tension in this additional cable becomes crucial to fix the torsion value, ensuring that all cables remain under tension, thus satisfying the tensegrity condition.

Future work aims to investigate the behaviour of the system approaches the singularity. In addition, it is suggested to explore the integration of springs in cables l_1, l_2 and l_3 to improve the stability of the system, especially during full rotation against gravity. Finally, the research is expected to investigate the replacement of the fourth cable with a leg as a potential design modification.

References

1. A. Weiss, A. K. Wortmeier, and B. Kubicek. Cobots in industry 4.0: A roadmap for future practice studies on human–robot collaboration. *IEEE Transactions on Human-Machine Systems*, 51(4):335–345, 2021.
2. E. Colgate, A. Bicchi, M. A. Peshkin, and J. E. Colgate. Safety for physical human-robot interaction. In *Springer handbook of robotics*, pages 1335–1348. 2008.
3. G. Michalos, S. Makris, P. Tsarouchi, T. Guasch, D. Kontovrakis, and G. Chryssolouris. Design considerations for safe human-robot collaborative workplaces. *Procedia CIrP*, 37:248–253, 2015.
4. R.B. Fuller. Tensile-integrity structures, 1962. Patent US3063521A. URL: https://patents.google.com/patent/US3063521A/en.
5. D.G. Emmerich. Construction of self-powered networks, 1964. French Patent No. 1,377,290.
6. K. D. Snelson. Tensegrity structures, 1965. U.S. Patent No. 3,169,611. Washington, DC: U.S. Patent and Trademark Office.
7. R. E. Skelton and M. C. De Oliveira. *Tensegrity systems*, volume 1. Springer, 2009.
8. Y. Liu, Q. Bi, X. Yue, J. Wu, B. Yang, and Y. Li. A review on tensegrity structures-based robots. *Mechanism and Machine Theory*, 168:104571, 2022.
9. K. Liu, J. Wu, G. H. Paulino, and H. J. Qi. Programmable deployment of tensegrity structures by stimulus-responsive polymers. *Scientific reports*, 7(1):3511, 2017.
10. M. Vespignani, J. M. Friesen, V. SunSpiral, and J. Bruce. Design of superball v2, a compliant tensegrity robot for absorbing large impacts. In *2018 IEEE/RSJ International Conference on Intelligent Robots and Systems (IROS)*, pages 2865–2871, October 2018.
11. J. M. Friesen, J. L. Dean, T. Bewley, and V. Sunspiral. A tensegrity-inspired compliant 3-dof compliant joint. In *2018 IEEE International Conference on Robotics and Automation (ICRA)*, pages 3301–3306, May 2018.
12. S. Ikemoto, K. Tsukamoto, and Y. Yoshimitsu. Development of a modular tensegrity robot arm capable of continuous bending. *Frontiers in Robotics and AI*, 8:774253, 2021.
13. R. W. Burkhardt. *A practical guide to tensegrity design*. Cambridge USA, 2008.

14. M. Arsenault and C. M. Gosselin. Kinematic and static analysis of a three-degree-of-freedom spatial modular tensegrity mechanism. *The International Journal of Robotics Research*, 27(8):951–966, 2008.
15. M. Q. Marshall. Analysis of tensegrity-based parallel platform devices. 2003. Doctoral dissertation, University of Florida.
16. Matthieu Furet and Philippe Wenger. Kinetostatic analysis and actuation strategy of a planar tensegrity 2-x manipulator. *ASME J. of Mechanisms and Robotics*, 11(6):060904, 2019.
17. Benjamin Fasquelle, Parag Khanna, Christine Chevallereau, Damien Chablat, Denis Creusot, Stephane Jolivet, Philippe Lemoine, and Philippe Wenger. Identification and control of a 3-x cable-driven manipulator inspired from the bird neck. *Journal of Mechanisms and Robotics*, pages 1–25, 2021.
18. J. M. Mirats-Tur and J. Camps. A three-dof actuated robot. *IEEE robotics & automation magazine*, 18(3):96–103, 2011.
19. Yong-Jae Kim, Jong-In Kim, and Wooseok Jang. Quaternion joint: Dexterous 3-dof joint representing quaternion motion for high-speed safe interaction. In *2018 IEEE/RSJ International Conference on Intelligent Robots and Systems (IROS)*, pages 935–942. IEEE, 2018.
20. I. John, S. Mohan, and P. Wenger. Kinetostatic analysis of a spatial cable-actuated variable stiffness joint. *Journal of Mechanisms and Robotics*, pages 1–21, 2023.
21. I. A. Bonev, D. Zlatanov, and C. M. Gosselin. Advantages of the modified euler angles in the design and control of pkms. pages 171–188, April 2002.
22. M. Stock and K. Miller. Optimal kinematic design of spatial parallel manipulators: application to linear delta robot. *J. Mech. Des.*, 125(2):292–301, 2003.
23. K. Muñoz, M. Porez, and P. Wenger. Review report - fourth quarter 2023: Analysis and design of spatial mechanisms of tensegrity for collaborative manipulation. 2024. Retrieved from `https://hal.science/hal-04405080`.